

The performance of bolt-reinforced and shotcreted in-stope pillar in rockburst-prone areas

Fhatuwani Sengani ^{a,*}

^a *Rock Engineering Department, Technical Services, South Deep Goldfields Mine, Johannesburg, South Africa*

Article History:

Received: 05 February 2018,

Revised: 28 April 2018,

Accepted: 11 May 2018.

ABSTRACT

Historically, the design of the in-stope pillar in underground excavations has been based on empirical formulae and numerical modeling. Although these design methods have been extensively applied in several gold mines in South Africa, rockburst, in-stope pillar burst/failure are continuously reported as the major problem faced by mines. Therefore, this study attempts to compare the performance of the shotcreted and bolt-reinforced in-stope pillar with the bolt-reinforced in-stope pillars. Numerical modeling was simulated focusing on the major principal stresses ahead and along the de-stress cuts, damage along the in-stope pillar (yieldability of the in-stope pillar), and the rate of energy release along the in-stope pillar. Owing to that, seismic events with $\log P \geq 1$ were used through assessing their source mechanism, damaged area, rock mass response after the event, and source parameters for the events. The results of the study have shown that the in-stope pillar along different de-stress cuts was extensively yielding in the model. Very high-stress magnitudes were forecast in a zone ahead of the advancing face. Further results from a seismic point of view have shown that the estimated source mechanism from different case studies had a dominant double-couple component, and the steeply dipping nodal plane aligns well with the NNE-SSW to the dike. Shear-type failure on the faults/dike was the most probable source mechanism of the events. Visually, observation results have shown that most of the bolt-reinforced in-stope pillars resulted in extensive scaling and fracturing during the dynamic movement of the ground, while bolt-reinforced and shotcreted in-stope pillars were noted to have minor or no damage during the dynamic movement of the ground.

Keywords : *Pillar burst, Seismic source mechanism, Numerical modeling, Pillar design*

1. Introduction

Zvarivadza and Sengani [25] define in-stope pillars as columns of unmined ore between two or more underground openings. Further study by Martin and Maybee [11], Sengani and Kataka [17], and Zvarivadza et al. [24] has indicated that these in-stope pillars are required to support the overburden and to provide a safe and stable working environment for mining personnel and equipment, and at the final stage of mining, most of the in-stope pillar can be extracted. In most underground mines in South Africa, pillars are arranged in a regular pattern or grids so as to simplify planning and operation. Owing to that, this pillar could be any shape – but mostly square or rectangular shape.

A previous study by Villaescusa [20] on geotechnical design for sublevel stoping has reported that pillar design and its stability analysis is one of the critical components of the stope design process. “Although the fundamental concepts of the factor of safety as the pillar strength/average pillar stress ratio and pillar stability have been understood for some time, it is only more recently that the tools have become available to allow more quantitative analyses of pillar strength and stability to be carried out” [20]. Further study by Salamon [16] Brady and Brown [1], and Villaescusa [20] went on and defined the term stability. Their study has expressed that the term stability in a rock mechanics point of view can be defined as the stability of equilibrium, or the ability of the overall structure, or an element of that structure (in the present case, a mine pillar) to undergo a small change in the equilibrium state of loading without producing a state of unstable equilibrium involving a sudden release of stored strain energy or large deformations.

1.1. Pillar stress-strain behavior

The understanding of stress and strain associated with in-stope pillar is significant when designing a stable pillar that can perform its function. The stress-strain curve of pillars is shown conceptually in Fig. 1. Ozbay and Ryder [13] explained the stress and strain curve in the sense that the initial straight line portion of the curve up to the yield point corresponds to the elastic response of the pillar, and the slope of this portion of the curve is the effective Young’s modulus of the pillar. The yield point indicates the onset of localized inelastic behavior or failure of some material in the pillar; however, after the yield point, a pillar is expected to exhibit strain hardening until the peak strength is reached. Load shedding then occurs until a residual strength is reached. Fig. 1 indicates the qualitative diagram of the complete stress-strain curve of a pillar.

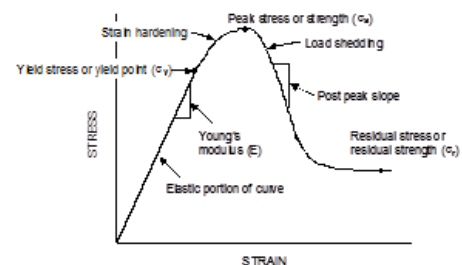


Fig. 1. A qualitative complete stress-strain curve [13].

Looking at the conduct of the pillar, the overall pillar bearing is controlled by the ratio of the pillar width to height. Different types of

* Corresponding author Tel: +27724430982. E-mail address: fhatugeorge@gmail.com (F. Sengani).

in-stope pillar failure at a different stress rate are based on the width-to-height ratio. Fig. 2 indicates the stress-strain behavior of various pillar types. It shows the change in behavior for different ranges of pillar width-to-height ratio.

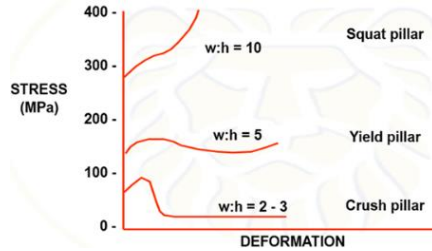


Fig. 2. Stress-strain curve for different types of in-stope pillar [13].

1.2. Pillar Design

A sound strategy for overall mine stability is critical to avoid accidents or conditions that may give rise to incidents. The major hazards addressed by a sound mining method design and layout include uncontrolled collapses of the mine or portion(s) thereof, surface subsidence, and major falls of ground incidents. A pillar support system is the chief basis of support in underground operations, especially in mines that use the room and pillar mining method. To design pillars for supporting mine openings, pillar strengths and pillar stresses need to be determined [22]. After determining pillar strengths and pillar stresses, separate pillars and pillar layouts will be designed depending on the degree of stability required.

Strength of pillars

According to Coates [2], the strength of the pillars depends on:

- The strength of the intact rock which makes the pillar material suitably downrated, taking into account the scale effect
- The geometry of the pillars, taking into account the shape and width-to-height ratio relationship

The strength of hard rock pillars is given in Equation 1 [14]:

$$P_s = K \cdot W_{eff}^{0.5} / H^{0.75} \quad (1)$$

Where: P_s = pillar strength

K = design rock mass strength (DRMS) in MPa

W_{eff} = effective pillar width

$W_{eff} = 4 \times \text{pillar area} / \text{pillar perimeter}$

According to Zvarivadza [23], the K value lies between a third of the Unconfined Compressive Stress (UCS) and the UCS. As the width-to-height ratio of a pillar decreases, the pillar gradually becomes weaker. The existence of joints in pillars will reduce pillar strength, since geological disturbances represent weaknesses [4]. Pillar monitoring is vital in any mining operation so as to avoid pillar robbing, thereby uncompromising the factor of safety (FOS). Measurements of mining heights together with pillar lengths and pillar widths will be used to determine the factor of safety of pillars as a means for monitoring pillars.

Pillar design procedure

Zvarivadza [23] pointed out that after determining the pillar strength and pillar stress, the FOS of the pillar can be calculated as follows:

$$\text{Pillar FOS} = \frac{P_{strength}}{P_{stress}} \quad (2)$$

The choice of the FOS value to be used for the design of the pillars and layout depends on the function of the pillars. Stope or panel pillars are required to provide stability to the section of stope between barrier pillars. The requirement for stability is therefore not as critical as that in barrier pillars, and occasional instability and failure of pillars is acceptable, provided that it does not compromise safety [22]. An indication of some instability is when spalling occurs from the pillar

sidewalls. The design principles are dependent on parameters such as rock strength and quality of the hanging wall rock mass. The minimum designed FOS of pillars is 1.6 for room and pillar platinum mines.

Because of the effect of the explosives used and bad ground conditions, the current practices of measuring the actual pillar dimensions in a bid to calculate the actual factor of safety are employed. The effect of stoping overbreak reduces the FOS, which increases the probability of failure. Apart from reducing the FOS, the effect of overbreak increases ore dilution, which affects revenues; hence, it is critical to review the literature of pillar cutting practices.

Empirical Rib Pillar Stability Chart

Hudyma [6] analyzed data from rib pillars in a number of Canadian open stope mines and plotted this in terms of the Y-axis (normalized pillar load to material UCS) and X-axis (pillar width/height). The database incorporated a wide variety of rock types and pillar loads that were derived from three-dimensional linear elastic numerical modeling. The data showed that squat pillars under low stress were stable (lower right quadrant in Fig. 3). Pillars become less stable as they move towards the upper left region. Hudyma divided the graph into three general zones: failed, transition, and stable. The database also included 13 case studies in which pillars were originally stable and subsequently yielded. These cases were observed to move correctly through the three zones on the graph. Hudyma also suggested that the graph could be used to predict pillar yield in open stoping design.

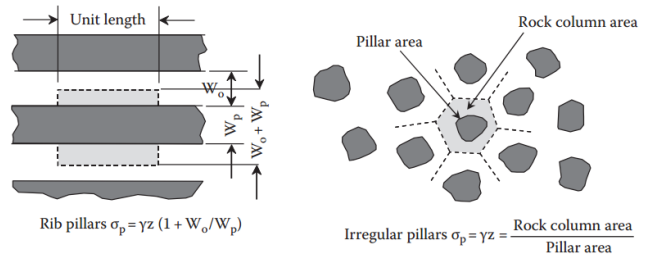


Fig. 3. Average vertical pillar stress in typical pillar layouts using equivalent area method plan views [5].

Numerical Modeling for Pillar Design

Both three-dimensional linear elastic and non-elastic numerical models can be used for pillar design. For linear elastic analysis, the three-dimensional stoping geometries can be represented in almost any required detail-incorporating sequencing. Elastic models are generally run as single material models, as the incorporation of multiple geological materials generally has a limited effect on the final stress outcome. Some models allow inclusion of a limited number of major geological discontinuities. The programs MAP3D [21] and Examine3D [15] are typical of the three-dimensional elastic numerical analysis software available. The output from such models is generally relatively straightforward to interpret with contours of principal stress and factor of safety often displayed.

2. Background of the study area

The mine is situated approximately 45 km west of Johannesburg and approximately 20 km south of Randfontein in the far West Rand Goldfield on the north-western rim of the Witwatersrand Basin. A previous study conducted by Joughin and Petho [8] has reported that the entire land acquired by the mine is approximately 3 563 hectares and also extends for approximately 9.5 km north-south and approximately 4.5 km east-west at its widest points. The mine consists of two shafts that are connected to each other.

2.1. Geology of the mine

Lithology above the mining area consists of the Pretoria Group sandstones, overlying the Malmani Dolomite, and the Ventorsdorp lavas of which the Ventorsdorp Contact Reef (VCR) forms the base [2, 9].

Only the VCR and Upper Elsburg Formation are of economic importance on mine [9]. Within the reef package, the stability of excavations is influenced mainly by the weak, argillaceous partings. These can form thin, potentially unstable beams in the hanging wall where they are closely spaced or inconveniently situated. They also weaken the rock mass, allowing more intense fracturing around excavations at great depths. In general, the argillaceous quartzite is weaker than siliceous quartzite and conglomerates. The shale units within the Kimberly Formation, particularly group 8 Unit, are extremely weak and contain cohesion and fewer discontinuities, requiring intensive support [3]. Fig. 4 illustrates the lithology of the mine. It shows their orientations in relation to the reef. The ore body dips towards the south and widens towards the east with a thickness of 2 m to approximately 130 m. The dip of the reef varies but is generally approximately 14°. There are different reefs that are mined as the depth of mining increases; however, all the reefs have different grain sizes, which have different grades, and the reef mainly consists of conglomerate.

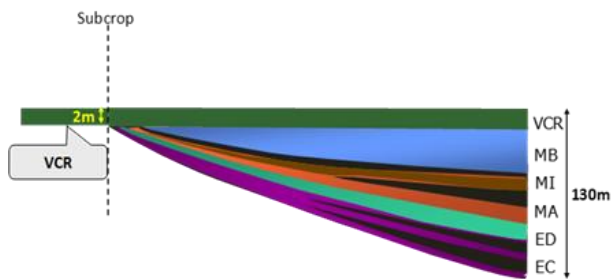


Fig. 4. West-east section of the ore body [25].

2.2. Mining method

The mining method that is used at the mine is the de-stress concept. This mining method relies on creating a zone of lower stress above and below the de-stress slot to allow Long Hole (LH) stoping to occur in a reduced stress window. The window is actually smaller, and the stress reduction is less than initially thought (see Fig. 5). There have been several de-stress layouts over time. The original corridor mining span was 240 m wide, with four corridors. The previous layout was named Low profile De-stress cuts. It was developed with a stoping height of 2.2 m, and the excavations were approximately 5 m wide and 10 m long. Subsequently, 5 m of the 10 m was backfilled to create a 5-m wide Strike Access Drive (SAD); thereafter, the adjacent excavation was mined in the same direction.

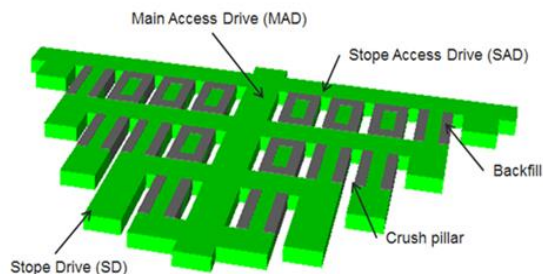


Fig. 5. Plan view of low profile de-stress layout.

The current de-stress design is called High-Profile De-stress cuts. This design has a mining span of approximately 180 m wide with six corridors. It was developed with a stoping height of 5.5 m, and the excavations are approximately 5 m with yield pillars of approximately 8 m wide and 20 m long. Each successive cut still has to be developed into a high-stress abutment. Stopping uses a centre out extraction sequence with backfill on each cut (see Fig. 6). The support installation is conducted through mechanical installation, and this support is capable of withstanding dynamic motions of the ground during seismic events.

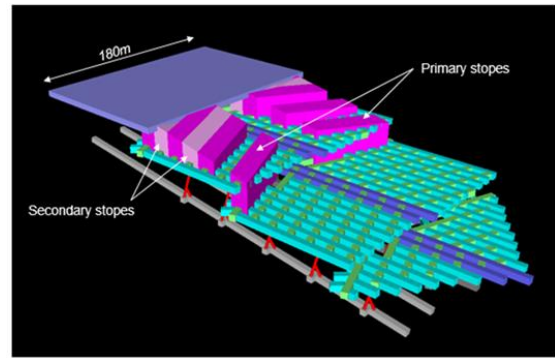


Fig. 6. Plan view of high-profile de-stress layout.

2.3. Virgin stress field and field stresses of the mine

To determine an accurate virgin (or primitive) stress tensor, stress measurements were carried out using strain gauge cells of the level in the vicinity of the shaft. The results of this exercise are presented in Table 1. Equation 1 represents the resolved virgin stress tensor used for numerical modeling. The orientation of the major principal stress is at a low angle to the dip of the strata, which promotes bedding parallel fracturing and beam buckling failure modes.

Table 1. Virgin principal stresses as measured 2 650 m below surface.

Principle Stress	Magnitude	Bearing	Dip
Major	80.8 MPa	144°	48°
Intermediate	58.9 MPa	359°	30°
Minor	36.3 MPa	265°	20°

$$\begin{pmatrix} \sigma_x & \tau_{xy} & \tau_{xz} \\ \tau_{yx} & \sigma_y & \tau_{yz} \\ \tau_{zx} & \tau_{zy} & \sigma_z \end{pmatrix} = \begin{pmatrix} 41.6 & -5.20 & -13.3 \\ -5.20 & 63.5 & 7.72 \\ -13.3 & 7.72 & 70.9 \end{pmatrix} \quad (1)$$

2.4. Seismicity of the mine and sensitivity and location accuracy of the seismic network

The seismic system is designed to run continuously and record seismic events whenever they occur. Ground vibrations caused by seismic events are recorded at each underground seismic site. These records are sent automatically to the Down Run Time System (DRTS). If the DRTS is down when a seismic event occurs, the data will be recorded in the seismometer and will, in most cases, be retrieved when the DRTS comes back online. Normally the DRTS requests seismic triggers, groups them into seismic events, and records the information on a hard disc.

The software program Egret (TM) is used to determine the system characteristics of seismic networks, through the sensitivity and the location accuracy. Egret can be used for:

- checking the performance of the seismic network;
- planning a new seismic network; and
- extension or modification of an existing network.

The sensitivity of a network is calculated using the empirical relationship between peak particle velocity (PPV), magnitude (or energy) of the event, and hypo-central distance. In determining the system characteristics, it was assumed that all geophones are functional and working properly. The sensitivity and location errors in XYZ were contoured on a plane dipping at 14° for the mine-wide network and on a flat plane at a representative point for the water barrier network. Most of the location errors occur in the direction normal to the plane defined by the positions of the geophones. Because of the installation of geophones close to the orebody, the largest errors occur in determining seismic event elevations. Fig. 7 shows that the sensitivity of the seismic network around the current mining areas is better than a magnitude equal to -1.5. Fig. 8 indicates that location errors are better when they are 30 m within the mine-wide network. Based on the sensitivity and location errors of the system, the seismic network system of the mine is

still considered to be a useful system.

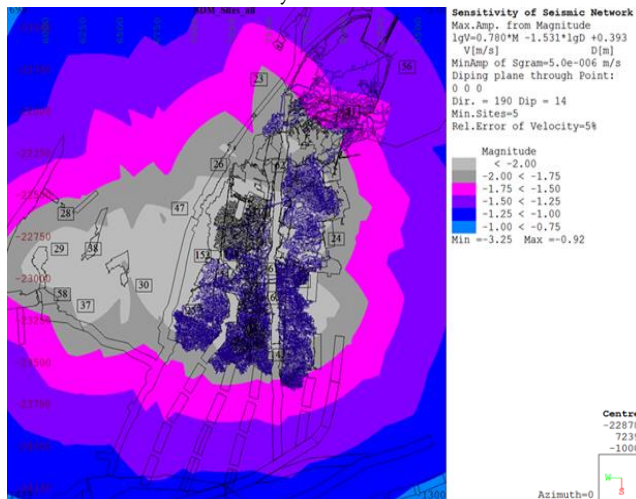


Fig 7. Sensitivity of the mine-wide seismic network.

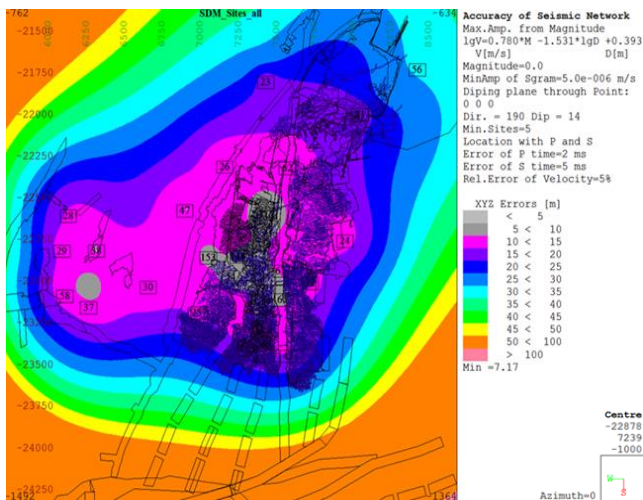


Fig 8. Location accuracy of the mine-wide seismic network.

2.5. Research problem

Rockbursts are considered to be the worst problems currently facing deep to ultra-deep gold mining in South Africa. This comes with other problems associated with it. The falls of ground (FOGs) and, to a larger extent, seismic activities, particularly near remnants and abutments, account for more than 50% of all mine fatalities in the South African gold mining industry. Over the past few years, there has been an improvement in the reduction of rock-related fatalities, injuries and seismic event rates through changes in the mining layout as well as support strategies. The in-stope pillar failure is still a major issue faced by the mines; therefore, this study was found critical so as to address or provide clarity on how to maintain the stability of the in-stope pillars in rockburst-prone areas.

2.6. Objectives of the study

The major objective of the study was to evaluate the performance of the in-stope pillar under dynamic conditions. This is done to achieve the major objective of the study-specific objectives that were set. These objectives include determining the rock mass damage, seismic potential and Rate of Energy Release at the vicinity of high-profile de-stress cuts, seismic source mechanism of the seismic events, seismic parameters, rock mass response during seismic events, and support performance during seismic events.

3. Research approach

3.1. Numerical modeling

The modeling workflow for this project was:

- all relevant geometric data were included in 3D CAD database using commercial software;
- discontinuum finite element (FE) mesh construction using commercial software and higher-order finite elements were used for all volume elements;
- assignment of geotechnical domains, material properties, initial conditions, boundary conditions and mining, and fill sequence to the FE mesh;
- solution of the stress, strain and displacement fields, and released elastic energy for each step in the modeled mining sequence using the Abaqus Explicit FE solver; and
- results processing, visualization and interpretation using commercial software and proprietary post-processing tools.

It should be noted that this project does not include re-calibration of the material properties and modeling of ground support elements. The Levkovitch-Reusch 2 (LR2) discontinuum constitutive framework was applied in Abaqus to describe the mechanical behavior of the rock mass and structures; however, the LR2 framework includes the following:

- Three-dimensional (3D) geometry, with excavations sequenced in a sufficient number of separate excavation steps to capture the necessary temporal resolution for the project scope, was used.
- Strain-softening dilatant constitutive model for the rock mass and structures with a generalized Hoek-Brown yield criterion was used. Different material properties were assigned to each geotechnical domain.
- Discontinuum formulation was implemented using cohesive finite elements to model discrete structures. Cohesive finite elements were free to dislocate and dilate and realistically capture the behavior of thin structures which tetrahedral finite elements which were not achieved as effectively. The complete interpreted structural model at the required resolution was included and, where appropriate, was supplemented with one or more discrete fracture networks (DFNs) to improve the structural resolution.
- Structures less persistent than those modeled explicitly were represented by “smearing” the effects of structures within the continuum regions of the modeled rock mass.
- Hydromechanical coupling was used, where necessary, to capture the effects of pore water pressure on the rock mass yield surface.

The LR2 modeling framework aimed for physical similitude, by making the fewest possible assumptions about the governing physics of the entire mine system within a single physics-based numerical model, at the required scale of the analysis. This results in a realistic but complex model, since complexity was the reality of all mines. Building a realistic mine model by including the governing physics means that realistic rock mass behavior evolves naturally in the model, and it is therefore essential for developing a detailed understanding of the likely rock mass behavior in response to mining.

3.2. Seismic source parameters and monitoring

In this study, seismic network systems were utilized in order to understand the seismic source mechanisms and damage related to large seismic events. To provide a meaningful analysis, seismic events with a magnitude greater than one were used. These were accompanied by the use of a common logarithm of seismic potency, $\log P$, so as to measure the magnitude of the seismic events at the mine. Hanks and Kanamori [7] have reported that the simplification of $\log P$ can be represented using a translation of $\log P$ to Hanks-Kanamori potency magnitude (mHK) = $(2/3) \log P + 0.92$. Magnitudes of seismic events at the mine

were calculated using the Hanks-Kanamori relation, which are listed in Table 2. For the research to be successful, case studies obtained from a deep to ultra-deep gold mine in South Africa were used.

Table 2. Hanks-Kanamori magnitudes for selected log P

log P	-2.0	-1.0	0.0	1.0	2.0	3.0	4.0	5.0
mHK	-0.41	0.25	0.92	1.59	2.25	2.92	3.59	4.25

Time-history analysis of the selected large events was analyzed. This was followed by location stability analysis, and then source mechanisms were analyzed. To evaluate location stability based on the uncertainty of the estimated source location, two factors were considered:

- Errors in the positions of the P- and S-waves arrivals; the errors were assumed to be normally distributed. The mean position and standard deviation were specified for all picks used in the location algorithm.
- Errors in the velocity model; the P- and S-wave velocity was assumed to have a normal distribution with a mean value (current P- and S-wave velocity) and a standard deviation (3% of the mean value).

Therefore, a Monte-Carlo simulation was performed to determine the effect of the aforementioned error distributions on the estimated event locations. The source mechanism was estimated using the amplitudes and directions of P- and S-waves recorded by the mine seismic sensors and source parameters. Synthetic and observed seismograms of different seismic events were also analyzed. Lastly, an underground observation after each event was conducted so as to identify the extent of damage and performance of the in-stope pillars.

4. Results of study

The results of the study are based on case studies comparing the impact of the presence and absence of shotcrete on the stability of the in-stope pillar when seismic events took place. The study compares the ground conditions and response of support system after seismic events took place along the in-stope pillar that was supported by Garford bolts with welded mesh and the in-stope pillars that supported both shotcrete and Garford bolts with welded mesh. First, numerical modeling results are discussed based on the in-stope pillar design, principal stress concentration, yieldability of the pillar, and Rate of Energy Release in the vicinity of the in-stope pillar. Moreover, support performance was simulated by the model; the performance was based on the plastic strain of the support units as mining progresses. These results were then followed by multiple case studies on the actual behavior of the in-stope pillars during seismic events. This section also provides details of the results and discussions on the seismic source parameter, time history of the events, location stability, and seismic source mechanism. Visual observation results on pillar performance are discussed. It should be noted that there are several case studies that could be discussed in this paper, but due to page limits and avoiding repetition of similar case studies, few case studies are discussed.

4.1. Stress simulation using numerical modeling and stress identification using core discing

Based on the results of the study, the model has shown high-stress magnitudes with $\sigma_1 = 300$ MPa in a narrow zone ahead of the high-profile de-stress cuts development. Owing to that, these developments appeared to be effective in providing the intended de-stressing effect. Further simulation has shown that the largest stress concentrations were developed on the flanks of the arrowhead, rather than ahead of the leading drive. This pattern indicated some potential to adjust the arrowhead geometry to achieve a more even stress distribution. Fig. 9 and Fig. 10 indicate the cross-section of the effectiveness of de-stressing between the cuts, without a significant stress channeling effect.

The concept of core discing was applied in order to verify modeling results. This concept has been extensively documented in different studies such as Lim and Martin [10], and Sengani and Zvarivadza [18] as one of the concepts that provide the correlation or relationship

between the disc thickness and fracturing variation with stress magnitude. However, Lim and Martin [10] and Sengani and Zvarivadza [18] have outlined that stress can be estimated based on the rate of disc crushing, wherein high stresses were associated with the extensively crushed core.

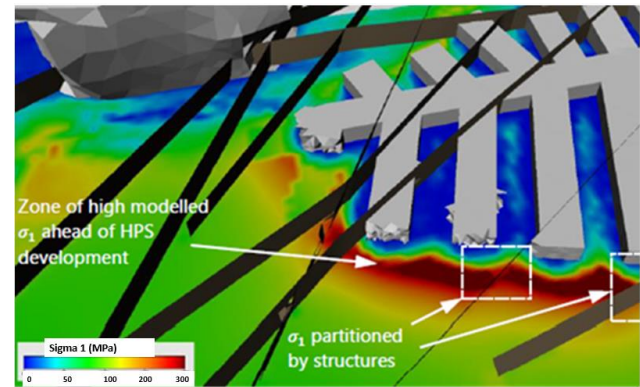


Fig. 9. Perspective views showing modeled σ_1 magnitude in one of the high-profile de-stress cuts. Faults shown in these figure have been clipped for clarity.

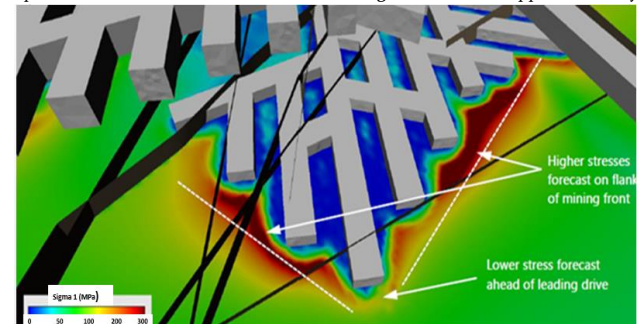


Fig. 10. Perspective views showing modeled σ_1 magnitude in one of the high-profile de-stress cuts.

Similar to other studies, it was noted that the cores that were recovered along the flanks of mining front were extensively crushed as compared to the core recovered ahead of the mining front (see Fig. 11 and Fig. 12). As a result, it was then confirmed that the simulated high stresses result from the model along the mining flanks and correlates with the actual behavior in underground excavations.



Fig. 11. Extensively crushed core recovered ahead of the mining flank.

4.2. Simulation on the yieldability of the in-stope pillar

The results of the model have shown that in-stope pillars were yielded throughout. Further results from the model have indicated high damage or failure to take place along seismic active geological structures. The model also simulates that the damage zone extends approximately half to one drive diameter in front of the mining front and the damage was partitioned by the faults. This partitioning arises because the stress was partitioned by faults and this inhomogeneous stress distribution leads to inhomogeneous damage distribution (see Figs. 13 and 14).



Fig. 12. Crushed core recovered ahead of the leading drive.

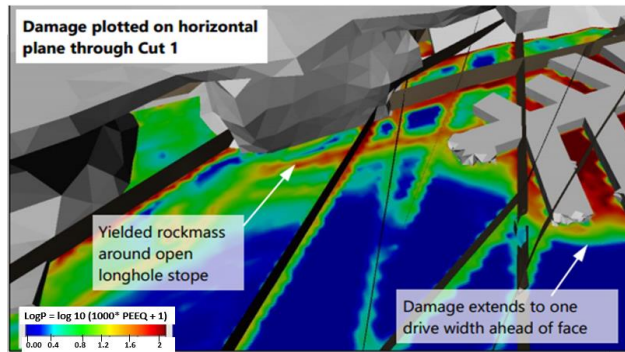


Fig. 13. Perspective views showing modeled rock mass damage.

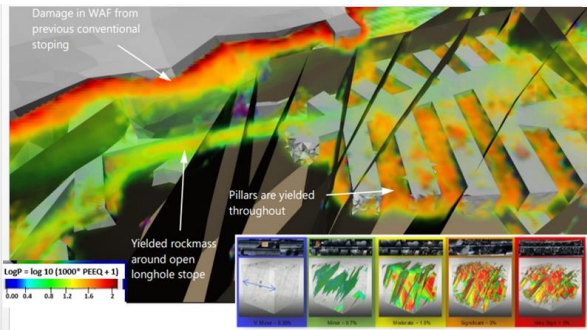


Fig. 14. Perspective views showing modeled rock mass damage. Faults shown in these images have been clipped for clarity.

4.3. Rate of energy release results

The FE model was used to simulate the rate of energy release (RER) for the yielding rock mass and for yielding structures along the high-profile de-stress cuts. However, both of these aspects contribute to seismic potential from, broadly speaking, strain bursts and fault slip events respectively. With seismic calibration, both forms of RER (rock mass and faults) can be used to establish correlations between seismic event clusters and RER, and can then be used to forecast seismic potential. Based on the results of the study, it was noted that the rock mass RER were concentrated in the newly formed yield pillars. This behavior appears to be a consequence of the intense yield that occurred as confinement was removed as the drives were developed under the high-induced stresses at the mining front (see Fig. 15). The location of the rock mass RER indicated a higher risk of strain bursting in the walls, rather than at the face, although this certainly does not rule out the possibility of face bursts. Appropriate measures (preconditioning practice and in-stope pillar) were still required to manage this risk (see Fig. 17). Furthermore, results have shown that fault-slip seismicity would be concentrated close to the mining front, within the cuts (see Fig. 17). This behavior, and the forecasts for rock mass RER discussed above, were evidenced to match the damage observations in some of the seismic damage that occurred along the high-profile de-stress cuts.

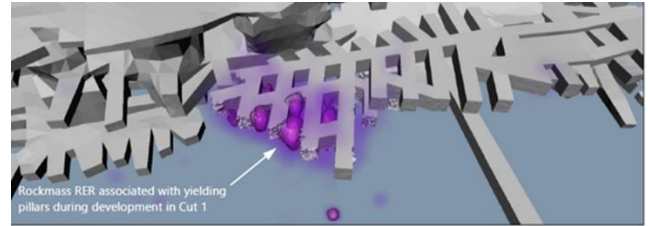


Fig. 15. RER concentrated in the newly formed yield pillars.

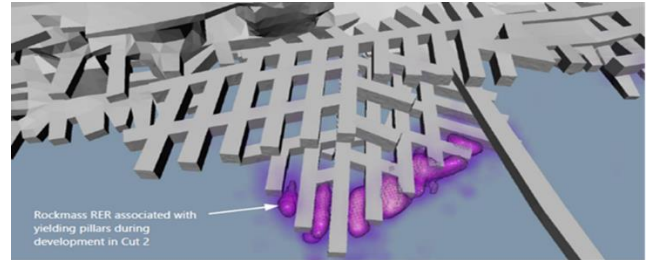


Fig. 16. RER concentrated ahead of the mining faces.



Fig. 17. Higher risk of strain bursting in the walls, rather than at the face.

4.4. Support performance using Abaqus numerical modeling software

Further results on support performance using numerical analysis have shown that the performance of Garford hybrid bolts was expected to be in a minimal plastic strain of approximately 5% of the development of de-stress cuts progress towards the end (see Fig. 18). However, this behavior was also evident in most in-stope pillars along the de-stress cuts owing to the fact that most of the deterioration of the support tendons were well pronounced in back areas/along seismic active geological structures and at the browns on long hole stope. For further reading on Garford hybrid bolt, a reader is referred to the study by Sengani [19] on a trial on Garford hybrid bolts performance in deep to ultra-deep gold mining. Further results on numerical analysis for the performance of the support tendons along the de-stress cuts have outlined that rapid failure of support performance should be expected when extensive extraction of long hole stopes are taken at the bottom, same and top de-stress cuts. Approximately 10% failure was simulated (see Fig. 19).

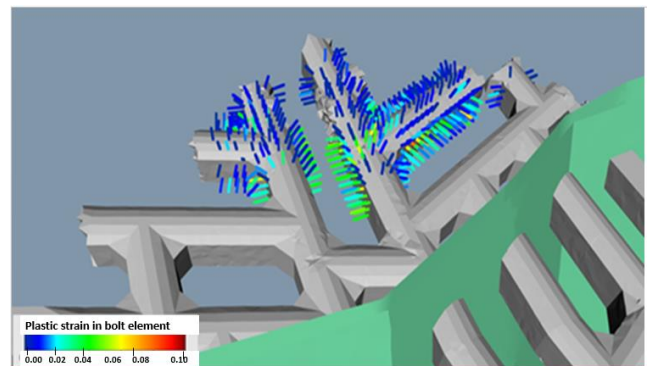


Fig. 18. Support performance at an early stage of mining.

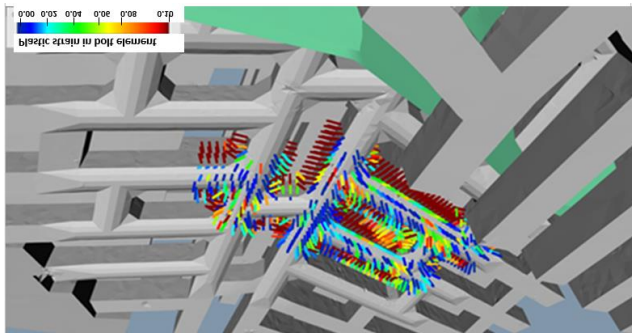


Fig. 19. Support performance when sequential stoping extraction progresses at a rapid rate.

4.5. Case studies: The behavior of bolt-reinforced in-stope pillar when subjected to seismic events

In this case study, 31 seismic events that occurred within the de-stress cuts were considered. Only seismic events with a magnitude greater than 1, which were recorded between 01 June 2015 and 09 December 2016, are considered. Most of these events were located at a distance between 10 m and 33 m from the closest working place. The PPVs of 0.055m/s to 0.2 m/s was observed at damage locations from within the recorded events. However, based on the scale developed at the mine, the PPV values were not expected to produce any severe damage; only falls of small loose rocks were expected. However, large damages were reported during the investigation. Fig. 20 shows the chart for the PPVs which are used at the mine.

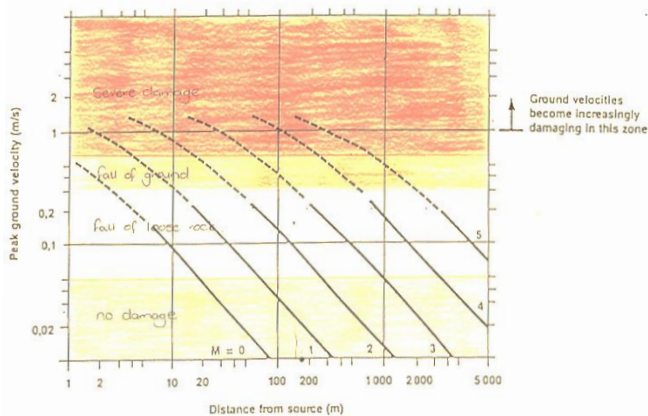


Fig. 20. PPVs scale used at the mine so as to determine or estimate whether the event should result in damage or not [12].

Case study 1

Two large seismic events were recorded in one of the de-stress polygons: a m1.1 event on 16 November 2016 at 15:13:37 (blue hourglass in Fig. 21) and a m1.9 event on 17 November 2016 at 09:24:59 (red hourglass in Fig. 21). Fig. 21 shows all m1>-3.5 events recorded during the day preceding the m1.1 event and the day following the m1.9 event; the events are represented by spheres colored by the time of occurrence and sized by local magnitude. The source parameters of both events are given in Tables 3 and 4.

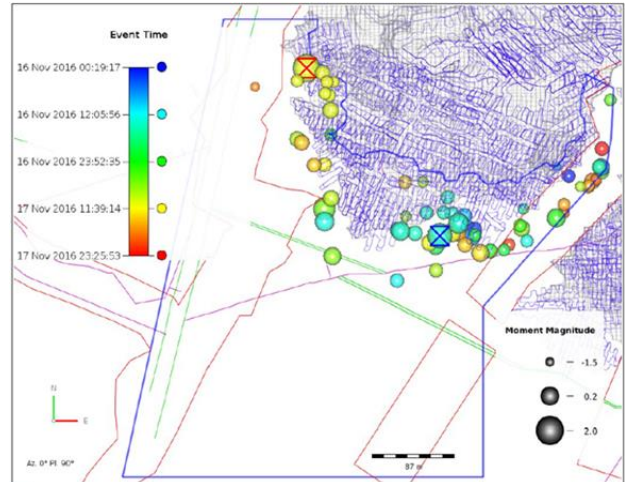


Fig. 21. All m1>3.5 seismic events recorded in C polygon between 16 November and 17 November 2016.

Time-history analysis

90-day time-history plots of all m1>2.5 seismic events were used. The results of the study have shown no significant trends prior to the m1.9 event, while they show a decrease in Schmidt number (see Fig. 22) and a corresponding increase in the activity rate before the m1.1 event (see Fig. 23). These temporal changes could be, but are not necessarily always, an indicator of rock mass instability, as similar trends have been observed in the past which were not associated with a large event being recorded.

Location stability

Similar to other case studies, the location stability analysis was performed using a Monte-Carlo simulation so as to determine the effect of the errors distribution on the estimated locations. The results of the study have shown that both events had an unstable location along the reef perpendicular axis due to the geometry of the seismic network. A polyhedron (corresponding to a 90% density iso-surface) of possible source locations is shown in Figs. 24 and 25.

Table 3: Source parameters of the m1.1 event

Parameter	Value	Parameter	Value	Parameter	Value	Parameter	Value
Time	03:24:23	Seismic moment [Nm]	3.0×10^{12}	Source size [m]*	120-210	Nodal plane one Dip [degrees]	50.8
Location:	7331.8	Radiated energy [J]	1.2×10^6	Static stress drop [MPa]	0.12	Nodal plane two Strike [degrees]	45.2
east	-23644.9						
north	-1034.2						
up							
Local magnitude, ml	1.1	Energy S / Energy P	1.1	Dynamic stress drop [MPa]	0.1	Nodal plane two Dip [degrees]	50
Potency [m3]	9.1	Corner frequency [Hz]	12.8	Nodal plane one Strike [degrees]	178.4		

Source mechanism

The estimated source mechanism of the m1.1 seismic event recorded on 16 November 2016 has a dominant double-couple component (42%). The steeply dipping nodal plane is parallel to the Corridor4 abutment as well as the general trend of faults in the region. The impulsive isotropic component (39%) suggests some interaction with stoping, and some closure in the nearby mine openings is plausible. The m1.9 seismic event recorded on 17 November 2016 has a dominant, normal double-couple component (81%). The nodal planes align with the NNE-SSW-

orientated structure west of the face, and the corresponding Es/Ep ratio (10.6) is consistent with a shear-type mechanism. It should be noted that the estimated mechanism is not stable and is very sensitive to input parameter changes or stations used during the inversion.

Stress modeling analysis

To compare the moment tensor results with the routine stress model, the maximum principal stress (Sigma1) vectors were calculated on the steeply dipping nodal planes. For the m1.1 seismic event, the Sigma1 vectors are near parallel to the plane in the region of the hypocenter (the

orientation of σ_{1max} is not consistent with shear-type failure). However, approximately 40 m down dip from the hypocenter, the orientation of the σ_{1max} vectors are similar to the P-axis of the moment tensor, and the stress orientation in this region is consistent with the shear-type failure mechanism suggested by the moment tensor inversion. Since this location (40 m down dip from the hypocenter) falls within the 90% confidence region of the location cloud, it is reasonable to conclude that the actual event location is deeper than that found through seismological processing (see Fig. 26).

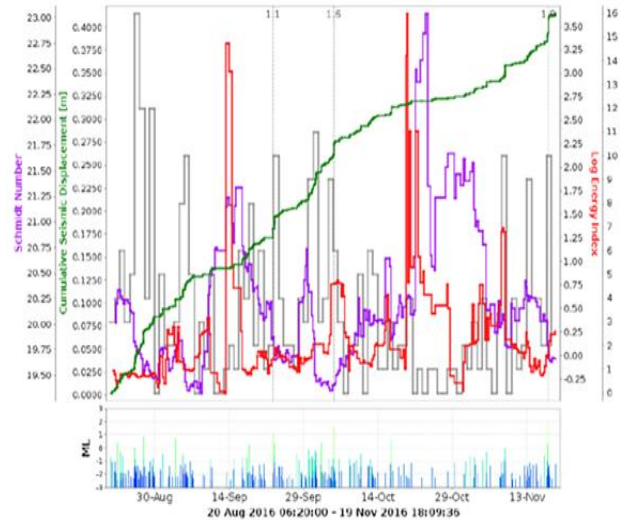


Fig.22. Time-history plot of the de-stress polygon associated with ml.9 event.

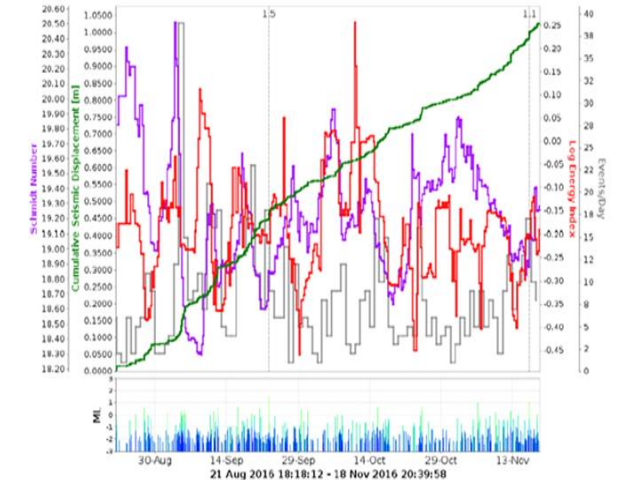


Fig. 23. Time-history plot of the de-stress polygon associated with ml.1 event.

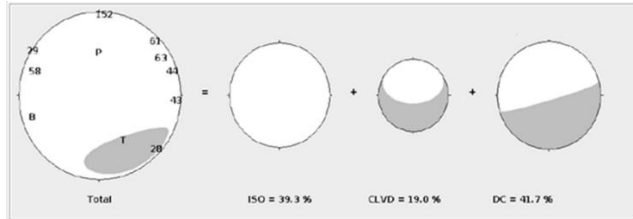


Fig. 24. The beach-ball decomposition of the estimated source mechanism for the ml.1 event.

Visual observations

Based on the underground investigation, it was found that all the in-stope pillars that were located closer to the source of the seismic events were associated with extensive scaling, pillar bursts, extensive fracturing and pillar budging along the full length, height and widths of the pillar. There was also a significant amount of broken rocks, both large and small in size, which fell out either through welded mesh or between the mesh overlap (see Fig. 27). More than 45 Garford bolts were pulled out

from the side walls of the in-stope pillars (see Fig. 26), and some of the bolts showed signs of yielding where ejection did not take place (see Fig. 27).

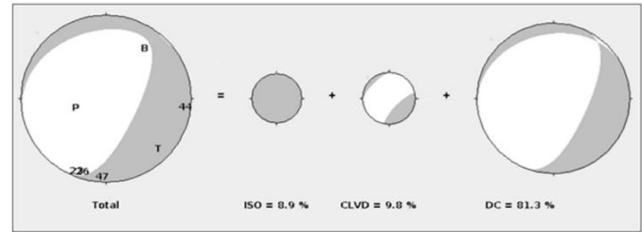


Fig. 25. The beach-ball decomposition of the estimated source mechanism for the ml.9 event.

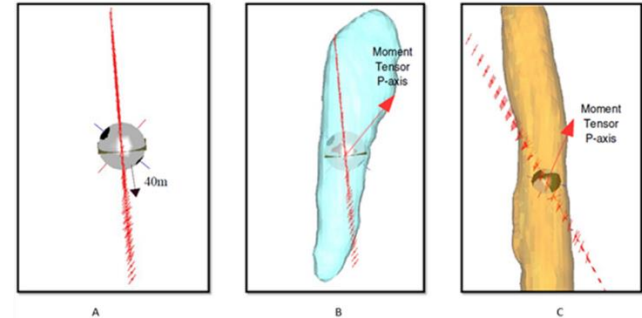


Fig. 26. A. Orientation of signal stress vectors on the steeply dipping nodal plane and of the ml.1 seismic event, B. Orientation of Signal stress vectors on the steeply dipping nodal plane of the ml.1 seismic event. Possible source locations are shown by a blue polyhedron. C. Orientation of Signal stress vectors on the steeply dipping.

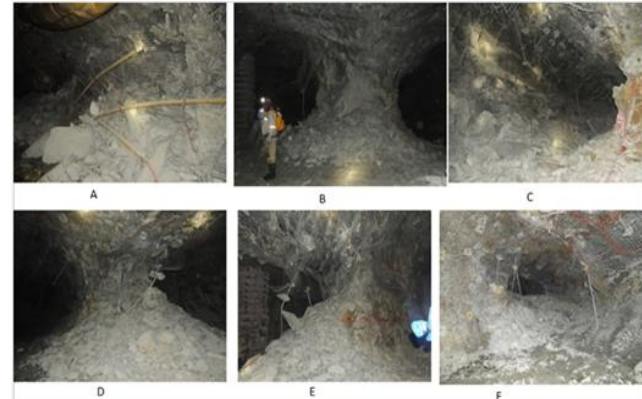


Fig. 27. Damage noted within the de-stress cuts after seismic events within the de-stress cut.



Fig. 28. Damage noted within the de-stress cuts after seismic events within the de-stress cut.

4.6. Case studies: The behavior of bolt-reinforced and shotcreted in-stope pillar when subjected to seismic events

More than 30 seismic events with a magnitude greater than 1 were also considered in this scenario. The PPVs were also recorded between 0.055m/s and 0.2 m/s. The main purpose of using seismic events with magnitudes greater than 1 was to generate a meaningful comparison of

the behavior of the in-stope pillars when supported by either bolt-reinforced only or bolt-reinforced with shotcrete.

A seismic event with a magnitude of $m_{l2.0}$ was recorded in one of the de-stress polygons (polygon A) at 03:24:23 on 22 August 2017. Historical data of seismic events recorded between 20 August 2017 and 22 August 2017 were plotted along the polygon so as to identify seismic activities before and after the main event (see Fig. 28). The $m_{l2.0}$ seismic event was located near the NNE-SSW orientation of one of the dike at the mine, and this event is represented by the orange hourglass. The aftershocks were located ahead of the mining face and align with the parallel stopping abutment. The source parameters of the $m_{l2.0}$ seismic event are given in Table 5.

Time-history analysis

Fig 31 shows a time-history plot of all $m_{l \geq 3.0}$ seismic events recorded in one of the de-stress polygons (blue outline in Fig. 31) since the beginning of July 2017. A medium-term decrease in Energy Index and the activity rate four days prior to the $m_{l2.0}$ seismic event was observed, but this trend might be an artifact of the low activity rate. No significant

temporal trends (e.g. sudden increase in activity rate) were observed before the occurrence of the large event.

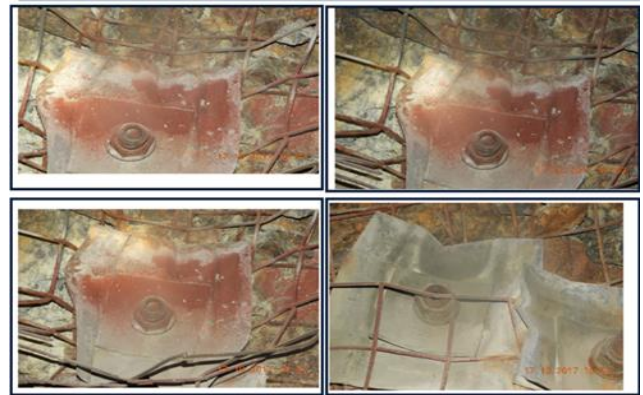


Fig. 29. Garford hybrid bolts showing an indication of yielding after seismic events.

Table 5: Source parameters of the $m_{l2.0}$ event

Parameter	Value	Parameter	Value	Parameter	Value	Parameter	Value
Time	03:24:23	Seismic moment [Nm]	1.3×10^{12}	Source size [m]*	100-180	Nodal plane one Dip [degrees]	66
Location:	6848	Radiated energy [J]	5.2×10^6	Static stress drop [MPa]	0.86	Nodal plane two Strike [degrees]	348
east	-23371.1					[degrees]	
north	-1096.8						
up							
Local magnitude, m_l	2.0	Energy S / Energy P	3.9	Dynamic stress drop [MPa]	3	Nodal plane two Dip [degrees]	24
Potency [m3]	4.0	Corner frequency [Hz]	15.1	Nodal plane one Strike [degrees]	171		

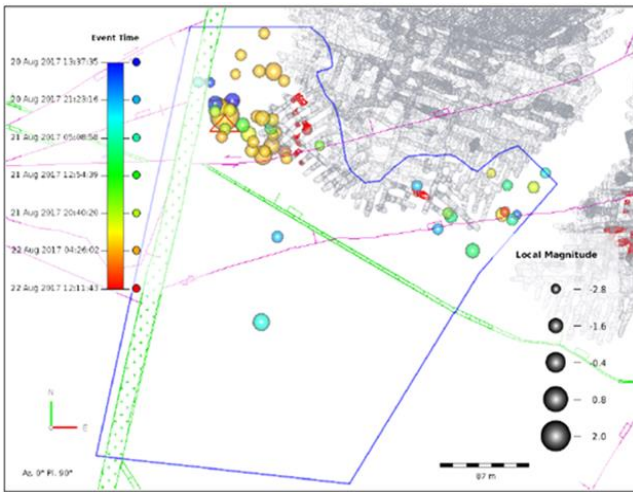


Fig. 30. Seismic events associated with one of the de-stress polygons at the mine.

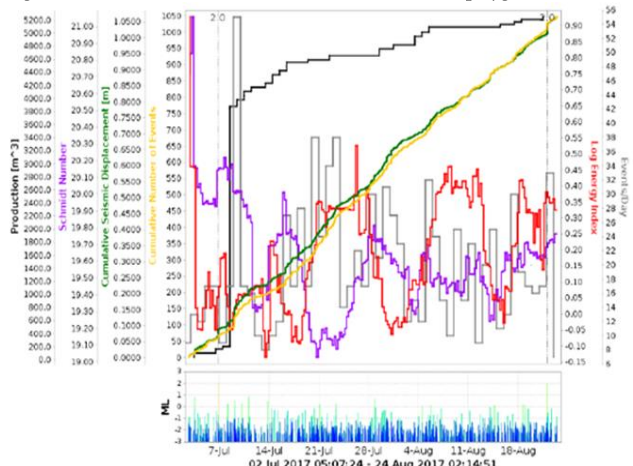


Fig. 31. Time-history plot of the de-stress cut polygon.

Location stability

To perform the location stability analysis, a Monte-Carlo simulation was performed to determine the effect of the errors distribution on the estimated locations. The results of the study have shown that the $m_{l2.0}$ seismic event was well constrained in the reef-parallel plane, and the corresponding location uncertainty was found to be less than 90 m. The event was not well constrained in the reef-perpendicular axis with a corresponding location uncertainty of 180 m. A polyhedron (corresponding to a 90% density iso-surface) of possible source locations is shown in Fig. 32.

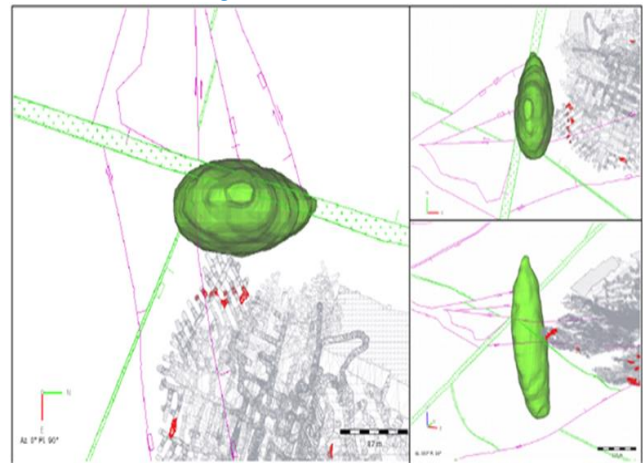


Fig. 32. Polyhedron of possible source locations in reef-perpendicular view (left), plan view (top right), and the oblique view (bottom right).

Source mechanism

The source mechanism was estimated using the amplitudes and directions of P- and S-waves recorded by the mine seismic sensors. The results of the estimation were shown in the form of a beach-ball plot in Fig. 33, and the corresponding nodal planes are shown in Fig. 34. A comparison of the observed and the synthetic seismograms is made. Fig. 34 has shown that the observed and synthetic seismograms were reasonably well correlated. The estimated source mechanism of the

ml2.0 seismic event was found to have a dominant double-couple component (72.7%), a small isotropic component (25.8%), and an almost negligible CLVD component (1.5%). The nodal plane has an N-S orientation and aligns well with the NNE-SSW-orientated to the dike, suggesting shear-type failure on dike as the most probable source mechanism of the ml2.0 event.

It must be noted that the accuracy of the moment tensor depends on the site orientations being correct. A site orientation inversion was recommended to be performed to ensure that the reliable moment tensors are calculated. The correct surveyed sensor positions are also vital in ensuring that accurate locations of events are calculated. This notation applies to all case studies.

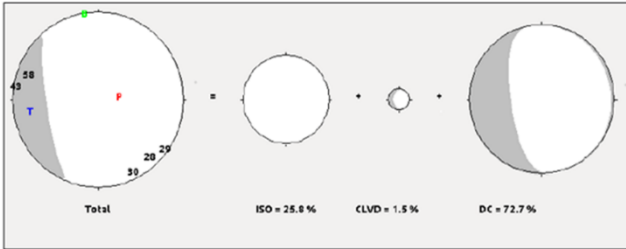


Fig. 33. Beach-ball plot of the estimated source mechanism of the ml2.0 seismic event.

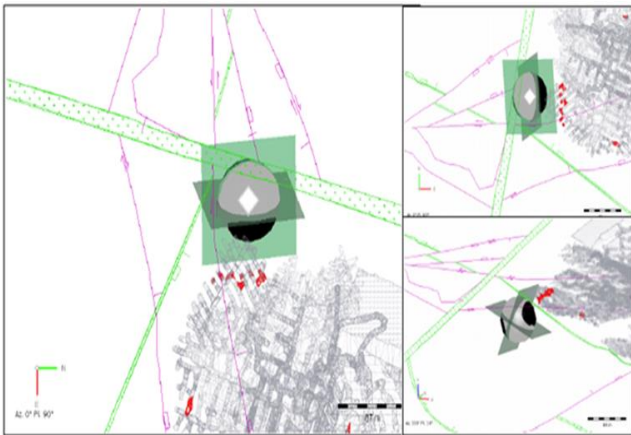


Fig. 34. Nodal planes of the estimated source mechanism in reef-perpendicular view (left), plan view (top right), and the oblique view (bottom right) of the ml2.0 seismic event.

Visual observations

During the investigation, none of the in-stope pillars were found to experience damage (see Fig. 35), although minor damage from the hanging wall and faces was noted. Based on the results of the scenario, it was clearly noted that the application of shotcrete fiber as support has adequately improved the performance of the in-stope pillar and also improved the safety of the employees that have to connect from one de-stress cut to another. Unlike in the first case study, the in-stope pillar was observed to be stable with no damage reported or noted along the in-stope pillar (see Fig. 36).

Case study 2

A seismic event with a magnitude of ml1.1 was recorded in one of the de-stress polygons (polygon B) at 09:43:15 on 02 August 2017. Historical

data of all ml>-3.0 events recorded seven days prior to the ml1.1 seismic event on 02 August 2017 were plotted along the polygon so as to identify seismic activities before and after the main event (see Fig. 35). The ml1.1 seismic event was located close to the NE-SW of the geological structure, and this event is represented by the orange hourglass. The source parameters of the ml2.0 seismic event are given in Table 6.



Fig. 35. In-stope with no damage after seismic events took place.



Fig. 36. In-stope with no damage after seismic events took place.

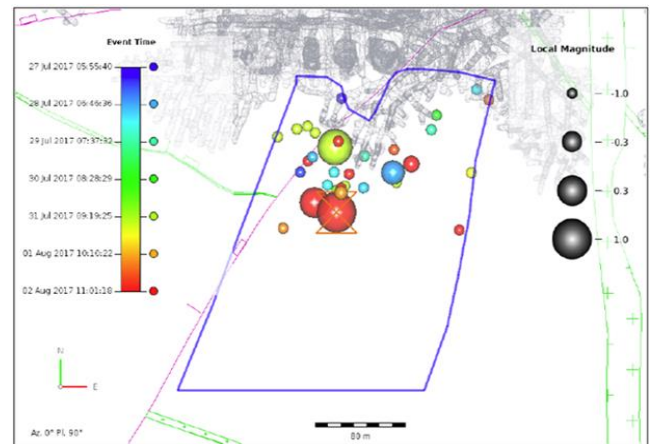


Fig. 37. Seismic events associated with polygon B at the mine.

Table 6: Source parameters of the ml1.1 event

Parameter	Value	Parameter	Value	Parameter	Value	Parameter	Value
Time	03:24:23	Seismic moment [Nm]	3.0×10^{12}	Source size [m]*	120-210	Nodal plane one Dip [degrees]	50.8
Location:	7331.8	Radiated energy [J]	1.2×10^6	Static stress drop [MPa]	0.12	Nodal plane two Strike [degrees]	45.2
east	-23644.9						
north	-1034.2						
up							
Local magnitude, ml	1.1	Energy S / Energy P	1.1	Dynamic stress drop [MPa]	0.1	Nodal plane two Dip [degrees]	50
Potency [m3]	9.1	Corner frequency [Hz]	12.8	Nodal plane one Strike [degrees]	178.4		

Time-history analysis

Fig. 9 shows a time-history plot of all $m \geq 3.0$ seismic events recorded in B polygon (blue outline in Fig. 38) since the beginning of July 2017. Two large events ($m \geq 1.0$) were recorded on 10 July 2017, resulting in an increase in seismic events and cumulative seismic displacement. Apart from a strong increase in activity rate (grey line in Fig. 9) associated with the m1.0 and m1.1 seismic events on 10 July 2017 and the anomalous increase observed between 22 and 24 July 2017, a relatively low average activity rate (~6 events per day) was observed in B polygon. A medium-term increase in the Schmidt Number (purple line in Fig. 38) was observed from 22 July 2017 prior to the m1.1 seismic event on 30 July 2017, but these temporal trends might be an artifact of the low activity rate. No significant short-term trends (sudden increase in activity rate, for example) were observed before the occurrence of the m1.1 seismic event.

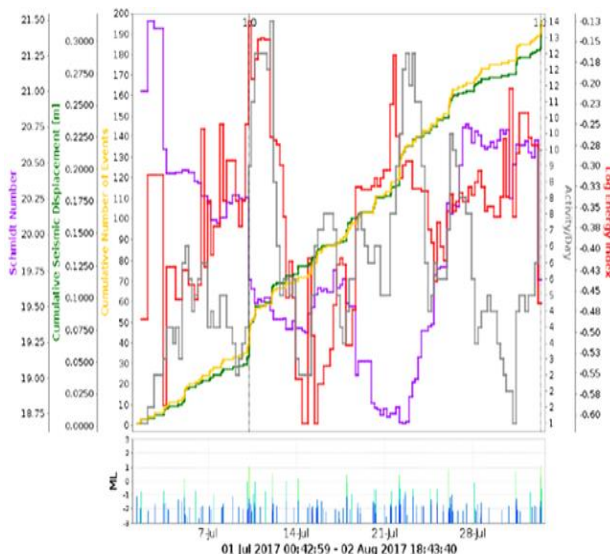


Fig. 38. Time-history plot of the B polygon.

Location stability

To perform the location stability analysis, a Monte-Carlo simulation was performed to determine the effect of the errors distribution on the estimated locations. The results of the study have shown that the m1.1 seismic event was well constrained in the reef-parallel plane, and the corresponding location uncertainty was found to be less than 60 m. The event was not well constrained in the reef-perpendicular axis with a corresponding location uncertainty of 225 m. A polyhedron (corresponding to a 90% density iso-surface) of possible source locations is shown in Fig. 39.

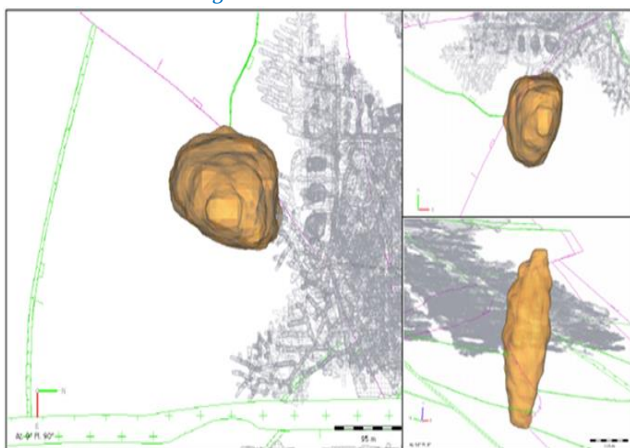


Fig. 39. Polyhedron of possible source locations in reef-perpendicular view (left), plan view (top right), and the oblique view (bottom right).

Source mechanism

The source mechanism was estimated using the amplitudes and directions of P- and S-waves recorded by the mine seismic sensors. The results of the estimation were shown in the form of a beach-ball plot in Fig. 40, and the corresponding nodal planes are shown in Fig. 40. A comparison of the observed and the synthetic seismograms was made. Fig. 41 has shown that the observed and synthetic seismograms were reasonably well correlated. The estimated source mechanism of the m1.1 seismic event was found to have a dominant double-couple component. The estimated source mechanism of the m1.1 seismic event has a dominant double-couple component (86.3%), a CLVD component (10.6%), and an almost negligible isotropic component (3.2%). The orientation of the nodal planes aligns with the NE-SW structure, suggesting shear-type failure on this structure as the most probable source mechanism of the m1.1 event.

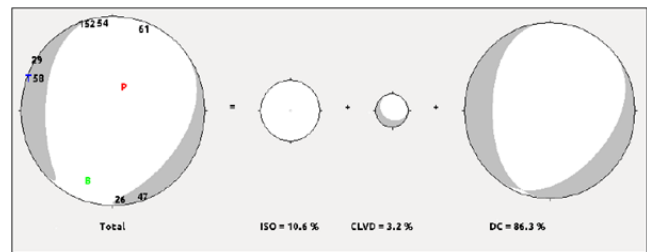


Fig. 40. Beach-ball plot of the estimated source mechanism of the m1.1 seismic event.

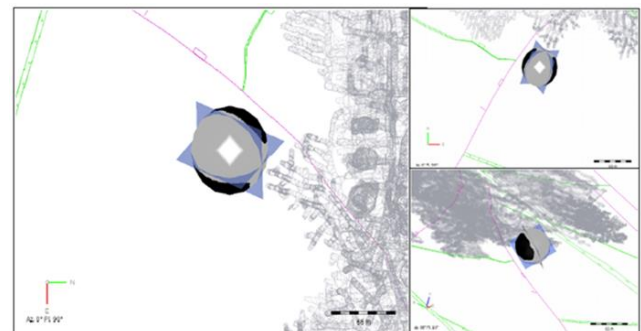


Fig. 41. Nodal planes of the estimated source mechanism in reef-perpendicular view (left), plan view (top right), and the oblique view (bottom right) of the m1.1 seismic event.

Visual observations

Similar to results of the first case study after the application of shotcrete, none of the in-stope pillars were found to experience damage (see Fig. 42), although a minor damage from the hanging wall and faces was noted.



Fig. 42. In-stope with no damage after seismic events took place.

Further study on the behavior of the in-stope pillar was validated using borehole logs. It was noted that the in-stope pillars which were

bolt-reinforced and shotcreted were moderately fractured with loose rocks contained within the in-stope pillar (see Fig. 43). On the hand, the in-stope pillars which were bolted only were noted to be highly fractured immediately after seismic events took place (see Fig. 44). The deterioration of the in-stope pillar was noted to be more rapid within the in-stope pillar that was supported by Garford bolts and welded wire only than that which was supported by Garford bolts with welded mesh and shotcrete.

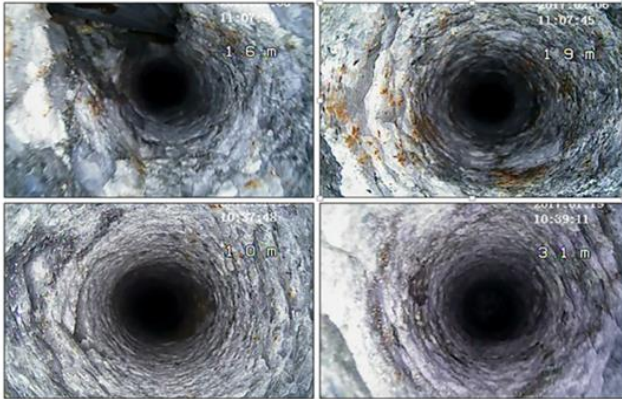


Fig. 43. Borehole log taken after the seismic event within the in-stope that was supported by primary and secondary supports.

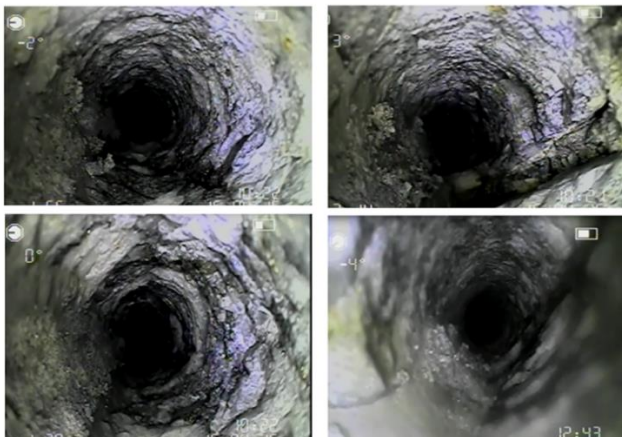


Fig. 44. Borehole log taken after a seismic event within the in-stope that was supported by primary support only.

5. Conclusions

Several case studies were considered, of which only four are presented in this paper. Based on the large quantity of data used, it was noted that the common source mechanism associated with large seismic events in deep-level gold mining in South Africa were slip-type events. Most of these events were dipping towards NNE-SSW or NESW. The estimated source mechanism of these events had a dominant double-couple mechanism. Results show that most of the damage was noted along the in-stope pillar at the mining faces. Therefore, it can be concluded that most of the events above a magnitude of 1 in deep-level gold mining are commonly influenced by the behavior and response of seismic active geological structures.

Based on the numerical modeling results and discussion of the study, the following conclusions were drawn: The model indicated that the yield pillars in high-profile de-stress cuts have yielded throughout. The model forecasts of high-stress concentrations with σ_1 up to ~ 300 MPa in a narrow zone ahead of the mining front were noted throughout high-profile de-stress cuts; this was also confirmed through the use of core discing concept. The concept has indicated that high stresses were experienced along the mining flank, while moderate stresses were experienced along the leading drives. These results were based on the crushing of the core discs. Lastly, the RER was noted to be concentrated

along the sidewall than the face of the mining faces. This was an indication that pillar bursts were expected to take place than facebursts. This does not mean facebursts might not be experienced. Pillar bursts were also noted along high-profile de-stress cuts. This indicated that the model results were correlating more with the actual behavior of the high-profile de-stress cuts on the ground.

The results of the study based on visual observations have indicated that most of the bolt-reinforced in-stope pillars resulted in extensive scaling and fracturing during the dynamic movement of the ground, while bolt-reinforced and shotcreted in-stope pillars were noted to have minor or no damage during the dynamic movement of the ground. Further analysis of the fracturing of the in-stope pillars was evaluated using a borehole log. It was noted that in-stope fractures were minor when the pillar was supported by both bolt-reinforcement and shotcrete fiber.

Acknowledgments

The author is grateful to Mr. Nin Nacker for his support and to the mine for facilitating the research.

REFERENCES

- [1] Brady, B. H. G. and Brown, E. T. 2004. Rock Mechanics for Underground Mining, 3rd edn., 628pp. Dordrecht, the Netherlands: Kluwer.
- [2] Coates, D., 1981. Rock Mechanics principles. 4th ed Ottawa: Department of Energy, Mines and Resources Canada.
- [3] De Kock, W.P. 1964. The geology and economic significance of west wits line. Geology of Some Ore Deposits in Southern Africa. (SH Haughton, Ed.). Geol. Soc. of S.Afr. Johannesburg.
- [4] Esterhuizen, G.S. (1995) Numerical studies of multiple reef stability pillars. Consultancy report, University of Pretoria.
- [5] Hoek, E. and Brown, E. T. 1980. Underground Excavations in Rock, 527pp. London, UK: IMM.
- [6] Hudyma, M. 1988. Development of empirical rib pillar failure criterion for open stope mining. MASC thesis, Department of Mining and Mineral Processing, University of British Columbia, Vancouver, British Columbia, Canada.
- [7] Hanks, T. C., and H. Kanamori. 1979, A moment magnitude scale, Journal of Geophysical Research, 84, 2348–2350.
- [8] Joughin, W.C and Petho, S.Z, 2007, South Deep regional modeling part I-design of regional pillars at South Deep Gold mine. Australian Centre for Geomechanics, pp579.
- [9] King, R.G, Jager, A.J, and Roberts, M.K.C.R. 1989. Rock mechanics aspects of stoping without back area support. COMRO Res. Rep. 17/89, Johannesburg.
- [10] Lim, S.S and Martin, C.D. 2010. Core diskings and its relationship with stress magnitude for Lac Du Bonnet granite. International Journal of rock mechanics and Mining science, 47(2): 254-264.
- [11] Martin, C.D and Maybee, W.G. 2000. The strength of hard-rock pillars. International Journal of Rock Mechanics and Mining Sciences, Vol. 37, no. 4, pp. 1239 – 1244.
- [12] Naicker. N. 2018. Evaluating seismic activities in deep level gold mine. Unpublished.
- [13] Ozbay, M.L. and Ryder, J.A. (1990) The effect of foundation damage on the performance of stabilising pillars, JI S. Afr. Inst. Min. Metall., Vol 90, No 2, pp 29-35.
- [14] Ozbay, M.L., Spottiswoode, S M And Ryder, J A (1993) A quantitative analysis of pillar-associated large seismic events in

- deep mines, Rockbursts and Seismicity in mines, Young (ed), Balkema, pp 107-110.
- [15] Rocscience Inc., 1990. Website: <http://www.rocscience.com/>.
- [16] Salamon, M. D. G. 1970. Stability, instability and the design of mine workings. *International Journal of Rock Mechanics and Mining Sciences*, 7(6): 613–631.
- [17] Sengani, F and Kataka M.O. 2017. A comparison of the effectiveness of the roof bolter and standard drill rig for installation of long anchors in hard-rock mines. 3rd young professional conference, SAIMM, 09-10 March 2017, pp 437 - 438.
- [18] Sengani. F and Zvarivadza.T (2018). Borehole periscope observations of rock fracturing ahead of the preconditioned mining faces in a deep level gold mine. First international conference on advances in rock mechanics, an ISRM specialized conference at Hammamet, Tunisia: ISBN: 978-9973-0929-0-8, 29-31 March 2018.
- [19] Sengani. F (2018). Trials of the Garford hybrid dynamic bolt reinforcement system at a deep level gold mine in South Africa. *Journal of the Southern African Institute of Mining and Metallurgy* 118(3):Pp293-296.
- [20] Villaescusa, E. 2014. Geotechnical design for sublevel open stoping. Taylor & Francis Group.
- [21] Wiles, T. D. 2006. Reliability of numerical modeling predictions. *International Journal of Rock Mechanics and Mining Sciences*, 43(3): 454–472.
- [22] Wilson, N.L, Oosthuizen, D.H., Brink, W.C.J., and Toens, P.D. 1964. The geology of Vaal Reef basin in the Klerksdorp area. *Geology of Some Ore Deposits in Southern Africa*. (SH Haughton, ed.). Geol.Soc.of S.Afr.Johannesburg.
- [23] Zvarivadza, T., 2012. Evaluation of Pillar Design Systems for Low Reef Platinum Mining. MSc Thesis. University of Wit-watersrand, Johannesburg, South Africa.
- [24] Zvarivadza, T., Sengani. F and Adoko. A. C (2017). In-stope pillar scaling and fracturing in Southern African deep level gold mines. 26th International Symposium on Mine Planning and Equipment Selection (MPES2017). 29 – 31 August 2017, Luleå, Sweden, pp. 379 – 388.
- [25] Zvarivadza. T and Sengani. F (2018). Calibration of yielding pillar performance in deep level gold mines. First international conference on advances in rock mechanics, an ISRM specialized conference at Hammamet, Tunisia: ISBN: 978-9973-0929-0-8, 29-31 March 2018.